# Fabrication of Suspended III−V Nanofoils by Inverse Metal-Assisted Chemical Etching of In$_{0.49}$Ga$_{0.51}$P/GaAs Heteroepitaxial Films

Thomas S. Wilhelm,[†,‡] Cody W. Soule,[§] Mohadeseh A. Baboli,[†,‡] Christopher J. O'Connell,[§] and Parsian K. Mohseni*,[†,‡]

[†]Microsystems Engineering, Rochester Institute of Technology, Rochester, New York 14623, United States
[‡]NanoPower Research Laboratory, Rochester Institute of Technology, Rochester, New York 14623, United States
[§]Microelectronic Engineering, Rochester Institute of Technology, Rochester, New York 14623, United States

**ABSTRACT:** Metal-assisted chemical etching (MacEtch) has been established as a low-cost, benchtop, and versatile method for large-scale fabrication of semiconductor nanostructures and has been heralded as an alternative to conventional top-down approaches such as reactive-ion etching. However, extension of this technique to ternary III−V compound semiconductor alloys and heteroepitaxial systems has remained relatively unexplored. Here, Au-assisted and inverse-progression MacEtch (I-MacEtch) of the heteroepitaxial In$_{0.49}$Ga$_{0.51}$P/GaAs material system is demonstrated, along with a method for fabricating suspended InGaP nanofoils of tunable thickness in solutions of hydrofluoric acid (HF) and hydrogen peroxide (H$_2$O$_2$). A comparison between Au- and Cr-patterned samples is used to demonstrate the catalytic role of Au in the observed etching behavior. Vertical etch rates for nominally undoped, p-type, and n-type InGaP are determined to be ∼9.7, ∼8.7, and ∼8.8 nm/min, respectively. The evolution of I-MacEtch in the InGaP/GaAs system is tracked, leading to the formation of nanocavities located at the center of off-metal windows. Upon nanocavity formation, additional localized mass-transport pathways to the underlying GaAs substrate permit its rapid dissolution. Differential etch rates between the epilayer and substrate are exploited in the fabrication of InGaP nanofoils that are suspended over micro-trenches formed in the GaAs substrate. A model is provided for the observed I-MacEtch mechanism, based on an overlap of neighboring injected hole distribution profiles. The nanofabrication methodology shown here can be applied to various heteroepitaxial III−V systems and can directly impact the conventional processing of device applications in photonics, optoelectronics, photovoltaics, and nanoelectronics.

**KEYWORDS:** InGaP, metal-assisted chemical etching, MacEtch, MACE, I-MacEtch, inverse-MacEtch, nanofoil
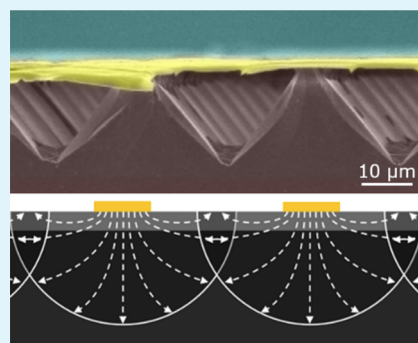
## 1. INTRODUCTION

Micro- and nanostructured semiconductor architectures have been an area of extensive study for years and are being incorporated into a wide variety of electronic and photonic devices due to their unique properties compared to their bulk counterparts.[1−4] Conventional top-down micro- and nanofabrication techniques include patterned wet-etching and reactive-ion etching (RIE); however, these methods can present challenges as desired features continue to move toward higher aspect-ratio geometries that are free of crystallographic defects.[5] Patterned wet-etching is more cost-effective in that it is solution-based and can be performed in conventional semiconductor wet benches, although it lacks the ability to yield high aspect-ratio structures due to it being isotropic or having crystallographic dependences.[6] In contrast, RIE is a dry-etching technique that can generate high aspect-ratio geometries at the expense of exposing the target material to high energy ion bombardment, which causes sidewall damage and detrimental lattice defects in addition to the intended material removal.[7,8] Moreover, RIE uses hazardous gases and is performed under high-vacuum conditions at elevated process temperatures,

making it less ideal for process simplification and cost reduction.[6]

Metal-assisted chemical etching (MacEtch, or "forward MacEtch" to distinguish it in later discussions) and inverse metal-assisted chemical etching (I-MacEtch) are top-down, solution-based fabrication methods that have been demonstrated as attractive alternatives for cost-effective generation of high aspect-ratio micro- and nanoscale semiconductor features.[1,6,9] These techniques have been gaining the attention of researchers in many fields, with structures generated for devices in a range of applications, including microfluidics,[10] biosensors,[11] photonics,[12,13] optoelectronics,[2,14] nanoelectronics,[15,16] energy storage,[17] and energy conversion.[18] The MacEtch technique was first formalized for Si in 2000,[19] and for the first III−V material (GaN) in 2002.[20] Research in this field has focused primarily on Si,[21−25] although several III−V materials, including GaN,[20,26] GaAs,[14,27−31] and GaP,[32] have

also been explored. Moreover, MacEtching of a ternary III−V alloy (i.e., InGaAs) has recently been reported for the first time by Kong et al.[33] The MacEtch mechanism relies on catalytic oxidation of a semiconductor substrate beneath a metal catalyst layer (e.g., Au, Ag, Pt, or Pd), and subsequent selective etching of the oxidized regions. A cathodic reaction occurs at the solution/metal interface, and includes oxidant reduction and injection of resulting holes (i.e., charge carrier transport) through the metal into the semiconductor at the metal/semiconductor interface. An anodic reaction then occurs at the metal/semiconductor interface that dissolves the oxidized material (i.e., mass transport of dissolution products).[6,9] MacEtch solutions consist of an oxidant such as hydrogen peroxide ($H_2O_2$) or potassium permanganate ($KMnO_4$), an acid such as hydrofluoric acid (HF) or sulfuric acid ($H_2SO_4$), and often a diluent or surfactant such as deionized water (DI-$H_2O$) or isopropyl alcohol (IPA). Hole injection is site-specific to the semiconductor regions interfaced with the metal and, in the conventional or forward MacEtch regime, preferential dissolution of oxidized material results in selective etching of the underlying substrate. Continuous catalytic oxidation and preferential dissolution causes the metal to sink into the substrate, such that the off-metal regions (i.e., the substrate regions not interfaced with the metal) remain intact.[6,9] Ordered arrays of structures are generated by patterning the metal using conventional semiconductor fabrication techniques, such as nanosphere lithography,[34,35] soft-lithography,[14,28] nanoimprint lithography,[36,37] photolithography,[38,39] or electron-beam lithography.[40,41]

The I-MacEtch process was formalized in 2015[42] and relies on many of the mechanisms described for the conventional MacEtch process (e.g., catalytic oxidation and preferential dissolution of selective regions). However, several mechanisms are fundamentally different. Most notably, the metal does not sink into the substrate as observed in forward MacEtch; instead, the metal acts as a patterned mask as well as a catalyst and generates inverse structures through preferential dissolution of off-metal regions.[32,42] As with forward MacEtch, a cathodic reaction occurs at the solution/metal interface, including oxidant reduction and hole injection through the metal and into the underlying semiconductor. However, as previously shown in the case of InP, distinct types of oxides are formed at the metal/semiconductor interface and in the off-metal regions.[42] These interfacial and noninterfacial oxides are nonsoluble and soluble in the I-MacEtch solution, respectively. The nonsoluble oxide layer generated at the metal-interfaced regions does not prevent the cathodic reaction (i.e., oxidant reduction and hole injection into the interfaced semiconductor), though it acts as a dissolution barrier by preventing the anodic reaction from occurring in these regions.[42] Without the anodic reaction and dissolution of the oxidized material occurring beneath the metal, the injected holes diffuse from the interfacial regions and oxidize the off-metal regions as well. With the off-metal regions oxidized to a state that is soluble in the I-MacEtch solution, mass transport or material dissolution occurs in regions where the semiconductor is not directly interfaced with metal. Therefore, submerging a metal-patterned sample in an I-MacEtch solution results in preferential etching of the off-metal regions, followed by etching of the oxidized regions underneath the metal as those regions become exposed.[32,42] The lateral and vertical etch rates (LER and VER, respectively) and maximum etch depth are tunable with the I-MacEtch solution, and with the size, pitch, thickness, and

type of metal catalyst.[42] However, the main obstacle for routine use of these metal-assisted catalytic etching techniques is the limited fundamental research into the various etching conditions (e.g., metal catalyst type, solution components, and the relative concentrations of each) for various semiconductor materials, particularly for ternary III−V semiconductors such as InGaP.

Ternary InGaP has important device applications in high electron mobility transistors (HEMTs)[43,44] due to its deep donor levels, high power density, and linearity, and it is a prominent III−V alloy in many tandem solar cell designs[45,46] due to its large band-gap energy and ability to be grown in a lattice-matched configuration with GaAs (i.e., $In_{0.49}Ga_{0.51}P$). Although catalytic etching of the binary components of InGaP (i.e., GaP and InP) has been reported,[32,42] MacEtch investigations involving the ternary phase have not been presented in the current literature. InP has been shown to exhibit I-MacEtch behavior,[42] while GaP has been reported to demonstrate both MacEtch and I-MatEtch tendencies based on the dimensions of the metal catalyst.[32] Given that InGaP, when lattice-matched to GaAs, has a ternary composition consisting of nearly equivalent In and Ga content, and since the individual binary constituents InP and GaP exhibit tendencies toward dissimilar metal-catalyzed etching modes, the dominant catalytic etching mechanism for InGaP is not immediately known (i.e., MacEtch or I-MacEtch).

Here, the metal-catalyzed etching behavior of lattice-matched heteroepitaxial $In_{0.49}Ga_{0.51}P$ films on GaAs(100) substrates is reported. A strong inverse-mode etching tendency is identified for InGaP, and the metal-catalyzed nature of the etching mechanism is revealed through a comparison of metallic masks with largely variant redox potentials. The vertical etch rates of nominally undoped, p-type, and n-type InGaP are quantified under well-controlled and fixed I-MacEtch conditions. The progression of the etch front over time is tracked, leading to localized etching of the InGaP epilayer and subsequent rapid dissolution of the underlying GaAs substrate as it becomes exposed to the I-MacEtch solution. Differential epilayer and substrate etch rates are exploited in the fabrication of suspended InGaP nanofoils of tunable thickness. Finally, a model is proposed for the InGaP/GaAs heterostructure I-MacEtch mechanism.

## 2. EXPERIMENTAL SECTION

All InGaP samples were grown on GaAs(100) substrates (WaferTech) using a 3 × 2″ Aixtron close-couple showerhead metal−organic chemical vapor deposition (MOCVD) reactor. Prior to growth, oxide desorption was performed at 835 °C under arsine ($AsH_3$) over a period of 10 min, after which the temperature was lowered to a growth set point temperature of 773 °C (equivalent surface temperature of 650 °C, based on LayTec EpiTT emissivity-corrected pyrometry measurements). Growth of $In_{0.49}Ga_{0.51}P$ with a thickness of 500 nm was carried out at a reactor pressure of 100 mbar. Trimethylindium [TMIn, $In(CH_3)_3$], trimethylgallium [TMGa, $Ga(CH_3)_3$], and phosphine ($PH_3$) were used as precursors for the supply of In, Ga, and P growth species, respectively. Doping was accomplished using disilane ($Si_2H_6$) for supply of Si dopants in n-type InGaP, and diethylzinc [DEZn, $(C_2H_5)_2Zn$] was used for supply of Zn dopants in p-InGaP samples. Dopant concentrations were determined as $n = 2 \times 10^{17}$ cm$^{-3}$ for InGaP:Si and $p = 5 \times 10^{16}$ cm$^{-3}$ for InGaP:Zn, based on post-growth Hall effect measurements (Nanometrics HL5500). For simplicity, nominally undoped InGaP will henceforth be referred to as i-InGaP.

After crystal growth, all wafers were submerged in diluted HF for native oxide removal, followed by degreasing with standard solvents.

Photolithography was used to pattern the samples; an adhesion promoter, hexamethyldisilazane (HMDS; MicroChemicals), and a positive g-line photoresist (Fujifilm HPR 504) were spin-coated, followed by a 100 °C soft-bake. Exposure and development were performed using a g-line stepper (GCA 6300) and CD-26 (Microposit), respectively. A 35 nm thick Au film was deposited by thermal evaporation (Lesker PVD75 Thermal Evaporator) at a rate of ∼1 Å/s, and liftoff was performed in an acetone bath with sonication. The size of each metal-patterned array was ∼2.5 × 2.5 mm$^2$, and they consisted of a mesh-shaped Au grid of ∼20 μm width separated by ∼10 × 10 μm$^2$ windows (henceforth, referred to as the "off-metal" regions). For consistency, only this pattern dimension is considered at length to establish the current I-MacEtch behavior of InGaP. Additionally, Cr-patterned samples were fabricated for comparison with Au-patterned samples. The Cr-deposited samples were patterned using the same photolithography process described above, and a Cr film with a thickness of 35 nm was deposited via thermal evaporation at a rate of ∼1 Å/s to achieve an identical pattern thickness, geometry, and dimensions as that described for Au.

All I-MacEtch experiments presented here were performed at room-temperature using a common solution of $H_2O_2$ with a molar concentration of 6.4 mol/L (to support the cathodic reaction and hole injection) and HF with a molar concentration of 14.1 mol/L (to facilitate the anodic reaction and material dissolution). All etching times are reported in the figure captions. Sample imaging was performed by scanning electron microscopy (SEM; Hitachi S-4000), and compositional mapping was carried out by energy dispersive X-ray spectroscopy (EDXS; TESCAN MIRA3 SEM).

## 3. RESULTS AND DISCUSSION

The set of tilted-view SEM images in Figure 1 illustrate the etch progression of Au-patterned i-InGaP samples etched for increasing lengths of time. Panels (e)−(h) (right-hand side) show higher magnification views corresponding to the image from the same row in panels (a)−(d), with the etch time increasing from the top to bottom in both columns. As observed, both the vertical etch depth and lateral etch width increase with time in off-metal regions. The same etching behavior has been observed in the case of InGaP samples patterned with Au mesh features of differing micron-scale dimensions. Regardless of whether the off-metal windows are small or large relative to the Au width shown in Figure 1, similar inverse etching behavior is found in the current micron-scale regime. Notably, Figure 1e−h shows that the Au/InGaP interface remains intact with increasing etch time. As indicated by the white arrow in Figure 1h, prolonged etching periods result in the formation of a submicron- or nanocavity (henceforth, referred to as a cavity) in the center of the off-metal region, indicating that the InGaP film is locally etched completely through.

Figure 1 indicates that InGaP exhibits an I-MacEtch behavior under the etching conditions employed here, causing preferential dissolution of the off-metal regions. Several possible explanations for the mechanism are proposed. As described above, the oxidant is reduced at the solution/Au interface and holes are injected along locations where InGaP is interfaced with Au. Similar to what has been reported by Kim et al. for I-MacEtch of InP,[42] the etching mechanism of InGaP observed here could imply the formation of distinct oxide layers in the Au-covered and off-metal InGaP regions that are nonsoluble and soluble in the I-MacEtch solution, respectively. In the case of InP I-MacEtch, the P-based interfacial oxide layer [i.e., $InPO_4$, $In(PO_3)_3$] remained insoluble in the etchant bath consisting of $H_2SO_4$ and $H_2O_2$, but was dissolved in HF after removal of the catalyst layer. Since the current work only
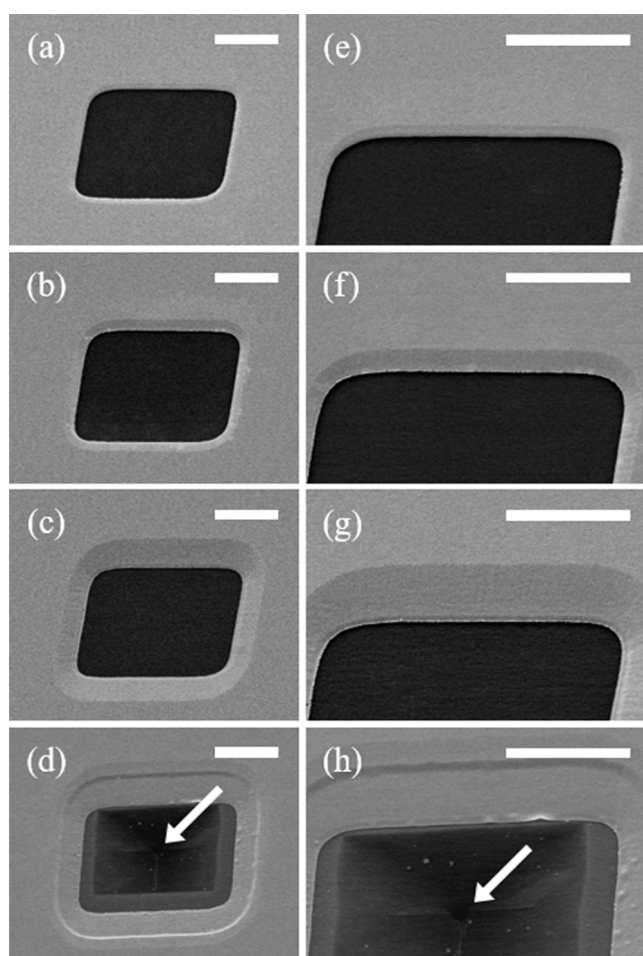


**Figure 1.** SEM images showing the etch progression of Au-patterned i-InGaP (initial thickness = 500 nm) with increasing time from the top to bottom. Panels (a) and (e) show a sample shortly after etching began after an etch time of 5 min. Panels (b) and (f) show the i-InGaP layer approximately halfway etched through after an etch time of 20 min. Panels (c) and (g) show a sample shortly before the i-InGaP layer has been etched through after an etch time of 40 min. Panels (d) and (h) show a sample immediately after the i-InGaP layer has been completely etched at the center of the off-metal window after an etch time of 50 min. The white arrows point to the location of the cavity. A suspended InGaP nanofoil has been formed in the regions surrounding the central cavity. All scale bars represent 4 μm.

employs HF, which has been shown to permit dissolution of the P-based oxides,[16,42] it is likely that the observed I-MacEtch mechanism for InGaP differs from that of InP.

Another possible explanation for the I-MacEtch behavior observed here could be related to the quality of the Au/InGaP interface and the hole distributions generated in the semiconductor from the cathodic reaction. In this case, holes are injected everywhere InGaP is interfaced with Au, but the Au layer is sufficiently thick (i.e., the 35 nm Au film is continuous and contains no voids) and wide (i.e., 20 μm Au grid width) such that it does not allow HF to access the oxidized InGaP regions covered by Au. Without solution access to the underlying InGaP regions, the anodic reaction is inhibited by the Au layer and material dissolution in metal-coated regions is prevented. As the cathodic reaction continues to inject holes that are free to diffuse from directly underneath the Au, extended hole distributions can form under the metal with profiles that are dependent on a variety of reaction- and

material-specific properties (e.g., magnitude of the reduction–oxidation potential relative to the ionization potential of the semiconductor, carrier mobility and diffusion length, temperature, etc.).[9,21,25] Under such conditions, the hole distributions from neighboring Au-coated regions may overlap and generate a higher hole concentration in these overlapped regions, leading to locally enhanced oxidation rates in the off-metal regions.[24] Thus, material dissolution of the exposed InGaP (i.e., oxidized off-metal regions) occurs first, and is followed by etching of the Au-covered InGaP adjacent to the off-metal regions as it becomes exposed. This explanation may be supported by the observation that the initial cavity formation is localized to the center of the off-metal window.

As seen throughout Figure 1, the Au layer continues to conform to the underlying etched InGaP in the interfacial regions, resulting in the Au/InGaP interface remaining intact. This is contrary to I-MacEtch behavior previously reported where the metal is suspended over the dissolved regions.[32,42] This observation may shed some light on the inverse etching mechanisms observed for InGaP. In the case where the catalyst layer is suspended over the etched regions, additional material volume is exposed underneath the Au as the off-metal regions continue to etch, allowing for mass transport pathways. In contrast, for the case where the metal conforms to the underlying profile, mass transport underneath the metal is impeded by a limited path for simultaneous HF access and material removal, thereby leading to reduced etch rates (discussed below). The limited path for solution access and mass transport of dissolved products is visible in Figure 1e−h as a narrow gap along the Au/InGaP interface at the window edge.

In order to validate the catalytic role of the metallic layer in the selective oxidation of $In_{0.49}Ga_{0.51}P$, etching investigations have been carried out using Au and Cr masks for comparison. A series of i-InGaP samples are patterned with Cr using the same preparation methods and etched under the same conditions as the Au-patterned InGaP, discussed above. The SEM images in panels (a) and (b) of Figure 2 show Cr-patterned InGaP
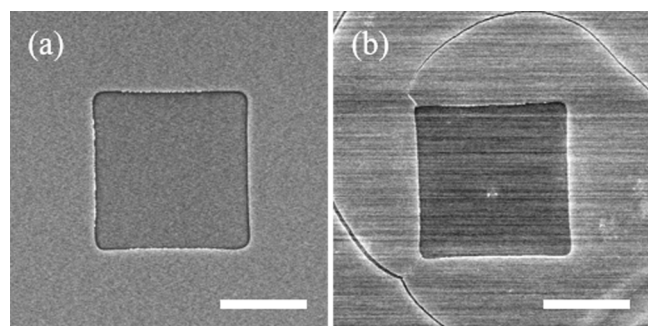


**Figure 2.** SEM images of Cr-patterned i-InGaP (a) before and (b) after being subjected to I-MacEtch for 50 min. Scale bars represent 5 $\mu$m.

samples prior to and after being subjected to I-MacEtch, respectively. In the case of the Cr/InGaP system, no observable etching is found; only deterioration of Cr mask is noted (visible cracks in metal layer), likely due to slow dissolution in HF.[47] This supports the understanding that the etching behavior of Au-patterned InGaP is metal-assisted and a consequence of catalytic oxidation, as further discussed below.

A necessary condition for the metal to serve as a catalyst in the redox reaction between $H_2O_2$ and the semiconductor is that

the redox potential of the metal must lie lower than the ionization potential (i.e., valence band edge) of the semiconductor.[21,48] Otherwise stated, in order to facilitate the requisite cathodic reaction, the reduction potential ($E^0$) of the metal must be offset relative to a more negative semiconductor ionization potential, when referenced to the standard hydrogen electrode (SHE). On this basis, while Au ($E^0$ = +1.50 V/SHE) is commonly used as a catalyst in standard Si MacEtch experiments, Cr ($E^0$ = −0.74 V/SHE) is known to prohibit catalytic etching.[21,49] Similar to the case of Si, InGaP has an ionization potential that lies intermediate to the redox potentials of Au and Cr.[50] Thus, a comparison between Au and Cr may determine whether an observed etching effect is simply due to patterned wet chemical etching, or if the metal promotes catalytic etching. Notably, Figures 2b and 1d show results obtained from identical InGaP samples (composition, thickness, and metal pattern geometry) that were etched under equivalent conditions (solution composition, temperature, and duration), with the only exception being the type of metal employed. Contrary to the case of the Cr/InGaP system (Figure 2), significant etching is observed in the case of the Au/InGaP system (Figure 1). This highlights the role of Au as a catalyst that enables a cathodic reaction for the injection of holes into the underlying InGaP film.

Progression of the vertical etch front in off-metal regions is considered next. Figure 3 shows VER data collected for InGaP samples of the three distinct doping types. The VER for i-InGaP, p-InGaP, and n-InGaP is determined to be 9.7 ± 0.7 nm/min, 8.7 ± 0.6 nm/min, and 8.8 ± 0.9 nm/min, respectively. Figure 3a shows the measured etch depth progression data for i-InGaP samples. A higher etch rate is observed initially (i.e., before 2.5 min) due to smaller volumes of oxidized material being consumed by the acid in the I-MacEtch solution near the sample surface. As etching progresses, greater volumes of oxidized material are exposed, and the VER of oxidized material is reduced in comparison to the initial nonlinear etching regime. Thus, beyond approximately 2.5 min etch time, an apparent linear etching regime is observed. A linear etch depth trend was also observed for p- and n-type InGaP samples. Kim and Oh have reported a similar linear I-MacEtch VER evolution (within measured error) during GaP micro-mesa fabrication.[32] In contrast, I-MacEtch of InP demonstrated a saturation of VER over time.[42] Despite the obvious distinctions between the current study and the experiments reported by Kim and Oh (e.g., catalyst type, thickness, geometry, etchant solution composition, etc.), which can explain the notable absolute VER differences, the common linear trend for InGaP and GaP may highlight an important difference between the I-MacEtch mechanisms of those systems in comparison to that of binary InP. The VER trend difference between InGaP and InP may potentially be related to the absence of a distinct undissolved oxide layer at the Au/InGaP interface, which was observed in the case of InP I-MacEtch. However, further analysis is required beyond the current study to clarify this point (discussed further below).

Figure 3b summarizes the representative VER for InGaP samples of all three doping types, which is defined as the measured slope of the etch depth vs etch time trend for each sample set in the linear etch regime. To ensure etch reproducibility and measurement repeatability, each depth data point (e.g., Figure 3a) was calculated as the mean value collected from at least 6 distinct samples etched for the same amount of time, and with at least 10 measurements per sample,
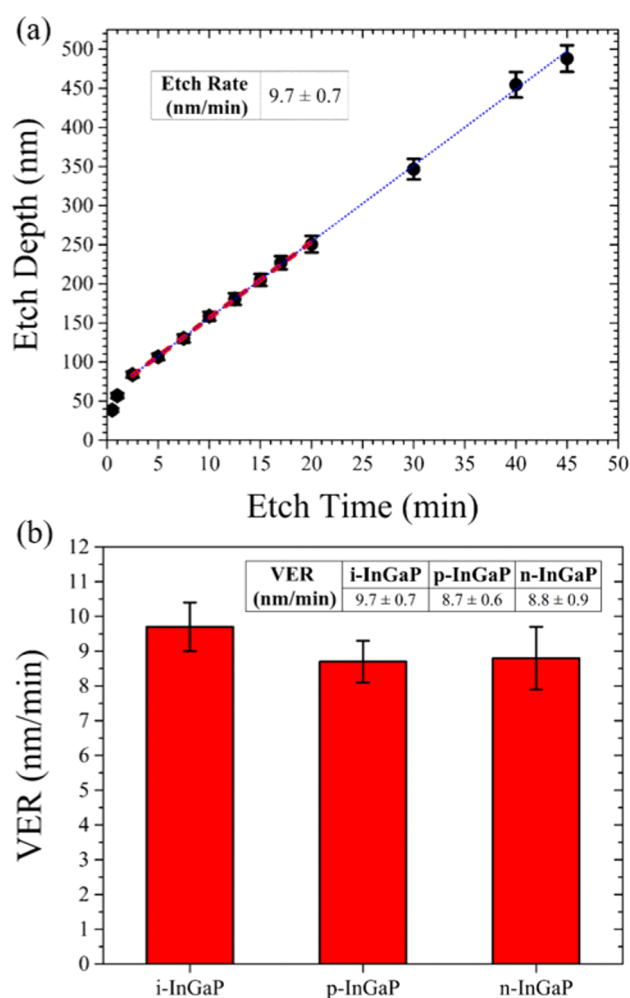
**Figure 3.** (a) Plot of vertical etch depth as a function of I-MacEtch time for i-InGaP. The red dashed line marks the linear regression from which VER is calculated. The blue dotted line shows an extrapolation of the linear regression for longer etch times and demonstrates that the constant etch rate persists for extended etch periods leading toward cavity formation. (b) Comparison of vertical etch rates (VER) for i-, p-, and n-type InGaP samples under common etching conditions.

based on cross-sectional SEM imaging. The error bars in Figure 3a represent the first standard deviation from the mean for depth measurements analyzed at a given etch time. Multiple etch times were analyzed to determine the overall etch rate (i.e., Figure 3b) for each doping type, based on the slope of a linear fit. Therefore, the data highlighted by the red dashed line in Figure 3a shows the linear regime from which the etch rate of i-InGaP was calculated to be $9.7 \pm 0.7$ nm/min. This linear regression is extended toward data points representative of longer etch durations by the blue dotted line in Figure 3a, which indicates a constant etch rate prior to the formation of cavities in the InGaP layer after approximately 50 min. In the limit of extended etch times required for the formation of cavities in the InGaP layer, the influence of the nonlinear etching regime (i.e., less than 2.5 min) becomes negligible. Thus, the linear regime marked by the red dashed line in Figure 3a was chosen for the calculation of etch rate because this constant etch rate is representative of the relevant etch depths of interest for the current study. Etch rates for n- and p-type InGaP were determined in the same manner.

In the I-MacEtch process, the catalyst or plane of hole injection does not sink, in contrast to forward MacEtch. In such a scenario, and due to the finite extent of oxidized material under the catalyst, a corresponding limit to catalytic etching will arise and lead to etch rate saturation, as reported in the case of InP I-MacEtch.[42] Under otherwise constant I-MacEtch conditions, InGaP samples of sufficient thickness (i.e., to prevent cavity formation) are expected to eventually experience such an etch rate saturation. In the current study, since thin InGaP films of 500 nm thickness are used, a saturation effect is not observed prior to cavity formation.

While a comparison of vertical etch rates between i-, n-, and p-type GaAs in the forward progression MacEtch regime has been previously reported,[14] no such comparison of etch rate dependences upon doping type has been presented to date (to the authors' knowledge) for I-MacEtch of III−V compounds. The current set of measurements have shown that InGaP VER in the I-MacEtch regime is independent of doping type, as all i-, p-, and n-type samples have shown comparable etch rates within the measured errors with no apparent trend favoring an enhanced etch rate for one type over another. In comparison to the I-MacEtch VER values reported for n-InP[42] and n-GaP,[32] the current study shows a reduced n-InGaP VER by a factor of ~0.44 and ~0.23, respectively. The etch rates reported here are also substantially lower than the I-MacEtch VER values presented by Lee et al. for n-GaAs under exposure to ultraviolet (UV) radiation (i.e., ~130 nm/min).[51] However, due to the large number of dissimilar experimental parameters across the listed set of most comparable studies (e.g., size, thickness, and type of catalyst features; conformal vs overhanging catalyst profile; ratio of catalyst area to off-metal area; dopant concentration; I-MacEtch solution composition; with or without UV exposure; etc.), direct I-MacEtch VER-to-composition correlations cannot be made.

In the absence of consistent VER comparisons in the I-MacEtch regime, etch rate dependences upon doping type are considered from literature pertaining to both III−V and Si systems in the forward MacEtch regime. For forward MacEtch of GaAs, consistently greater VER values were observed for p-type samples, independent of etchant temperature, dilution ratio, and oxidant concentration.[14] In contrast, Lai et al. have shown that, for forward MacEtch of Si in solutions with comparable HF proportions of $\rho = [HF]/\{[HF] + [H_2O_2]\} = 0.68$ as in the current study, p-type samples showed reduced etch rates relative to n-type Si, by a factor of ~0.85.[25] In the case of Si, the lower forward MacEtch rate of p-type samples can be attributed to Schottky barrier-induced hole drift away from the metal/semiconductor interface. However, the same explanation cannot hold for the current InGaP I-MacEtch study, since the etch front progresses in off-metal areas and evidence for preferential localization of hole distributions at the Au/n-InGaP interface (i.e., forward MacEtch) has not been observed. Therefore, the VER of InGaP in the I-MacEtch regime appears to be independent of differences in Fermi energy and workfunction. This is consistent with the model for metal-catalyzed etching whereby the offset between metal redox potential and semiconductor ionization energy is more critical than the availability and type of free carriers.[21,48]

Next, the heterostructure I-MacEtch stage is considered. Figure 1d,h shows SEM images obtained immediately after the InGaP layer has been locally etched through, marked by the formation of a cavity in the center of the off-metal window (indicated by a white arrow in Figure 1d,h). The InGaP layer

becomes progressively thinner toward the center of the window, with an ultrathin InGaP nanofoil surrounding the cavity location. The nanofoil thickness is tunable with etch time, and Figure 1d shows the nanofoil suspended above a trench formed in the underlying substrate. The microscale trench underneath the overhanging InGaP nanofoil is formed by the rapid dissolution of the GaAs substrate, which is accommodated by HF access and mass transport pathways through the cavity. The SEM images in Figure 4 show the
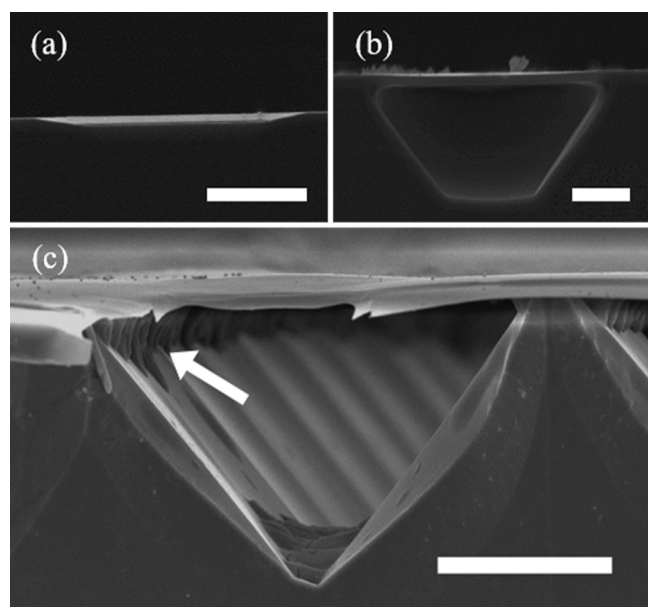


**Figure 4.** Cross-sectional SEM images of Au-patterned i-InGaP showing a sample (a) before central cavity generation (etch time of 20 min) and (b, c) after central cavity generation and formation of the suspended InGaP foil (after an etch time of 50 min). A cross-sectional view of an ordered array of GaAs micro-trenches and suspended InGaP nanofoils with re-entrant profiles in the GaAs substrate indicated by the white arrow is shown in (c). The Au layer is observed on top of the suspended InGaP foil at the sample surface. Scale bars in (a, b) represent 2 $\mu$m, and in (c) represent 10 $\mu$m.

cross-sectional view of etch progression through the InGaP film for i-InGaP samples. Figure 4a shows an example of a sample that has been subjected to the I-MacEtch solution, though prior to the time of cavity formation; thus, the InGaP film has not yet been etched through. Alternatively, Figure 4b shows a cross-sectional view of a sample subjected to I-MacEtch beyond the point of cavity formation, wherein a micro-trench is generated in the GaAs substrate underneath the InGaP window. Figure 4c illustrates the ordered pattern of dissolved GaAs micro-trenches directly below the center of each window in the array. It should be noted that Figure 4b was not cleaved at the center of the window for cross-sectional imaging, which explains why a centrally located cavity is not apparent in the InGaP layer along the imaging plane and why the trench in the underlying GaAs does not converge to a point at the base (i.e., an inverse pyramid shape). As described above, holes are injected through the metal and into the underlying semiconductor throughout the entire etching process such that hole diffusion forms a hemispherical distribution around each injection site. An interesting consequence of subjecting heteroepitaxial samples to such an I-MacEtch process is the differential catalytic oxidation of the epilayer and the underlying substrate. If the

hole diffusion length is greater than the thickness of the epitaxial layer, then the substrate will be continuously oxidized while the epitaxial layer is being etched. The hole distribution is likely to differ from layer to layer based on the material properties; however, an important observation is that, without HF access to the underlying oxidized substrate for material dissolution, the substrate becomes heavily oxidized until it reaches a saturation point. Here, with the GaAs substrate being heavily oxidized throughout the InGaP etching phase, upon cavity formation in the epilayers, a rapid dissolution of GaAs is observed with a vertical etch rate of approximately 9 $\mu$m/min.

The post-I-MacEtch nanofoil heterostructure is more clearly revealed via EDXS mapping. Figure 5a shows a cross-sectional SEM image of an i-InGaP sample (i.e., 500 nm i-InGaP film on a GaAs substrate), with a corresponding set of EDXS maps representative of elemental In, Ga, Au, P, and As shown in panels (b)−(f), indicating the composition of the final nanofoil structure. Figure 5d shows the presence of the Au catalyst layer on the surface of the sample. Panels (b), (c), and (e) show the InGaP layer in the same vicinity as the Au film, and panels (c) and (f) show the GaAs substrate underneath the InGaP film. It is noted that Au, In, and P are only present along the nanofoil near the surface of the sample. Elemental As is only detected beneath this layer, corresponding to the location of the GaAs substrate, and Ga is detected in both the InGaP layer and GaAs substrate, as anticipated. Figures 4b and 5a indicate the etch front in the GaAs substrate progresses along the {111} planes [i.e., micro-trench sidewalls are oriented 54.7° relative to the (100) substrate surface plane], which suggests crystallographically preferential etching occurs in the GaAs substrate with the InGaP window acting as a patterned mask. The etching behavior along the GaAs{111} planes agrees with the conventional selective chemical etching behavior of GaAs,[52] including the re-entrant profile at the intersection of the InGaP nanofoil and the GaAs{111} planes seen in Figures 4c and 5a (indicated by white arrows). While the GaAs substrate exhibits masked chemical etching behavior, enhanced etch rates are expected during the early stages of GaAs dissolution, and corresponding to etch depths equal to the hole diffusion length (i.e., the oxidation range in the I-MacEtch regime). The distinct etch rates and etch progression behavior between the InGaP film and the GaAs substrate demonstrates the advantage of utilizing dissimilar oxidation effects and hole distributions in heteroepitaxial systems for the formation of suspended structures. In the current study, beyond the point of cavity formation by I-MacEtch, the etch rate of GaAs is sufficiently high in comparison to InGaP to allow for the formation of suspended nanofoils.

The schematic illustrations shown in Figure 6 depict the Au/InGaP/GaAs I-MacEtch mechanisms, processes, and resulting structures. Figure 6a is a model of the mechanisms and reactions that occur during I-MacEtch. First, a cathodic reaction occurs with oxidant reduction at the solution/Au interface (black arrow), accompanied by hole injection into the underlying semiconductor at the Au/InGaP interface (blue arrow). An anodic reaction occurs with the dissolution of oxidized off-metal regions (red arrow). The catalytic etching behavior of InGaP, as observed here, can be understood in terms of hole distributions corresponding to adjacent injection sites (i.e., metal/semiconductor interfacial regions). Figure 6b depicts hole distributions as regions marked by white dashed arrows, resulting from the catalytic oxidation at neighboring Au locations. The hole distributions and oxidation profiles can
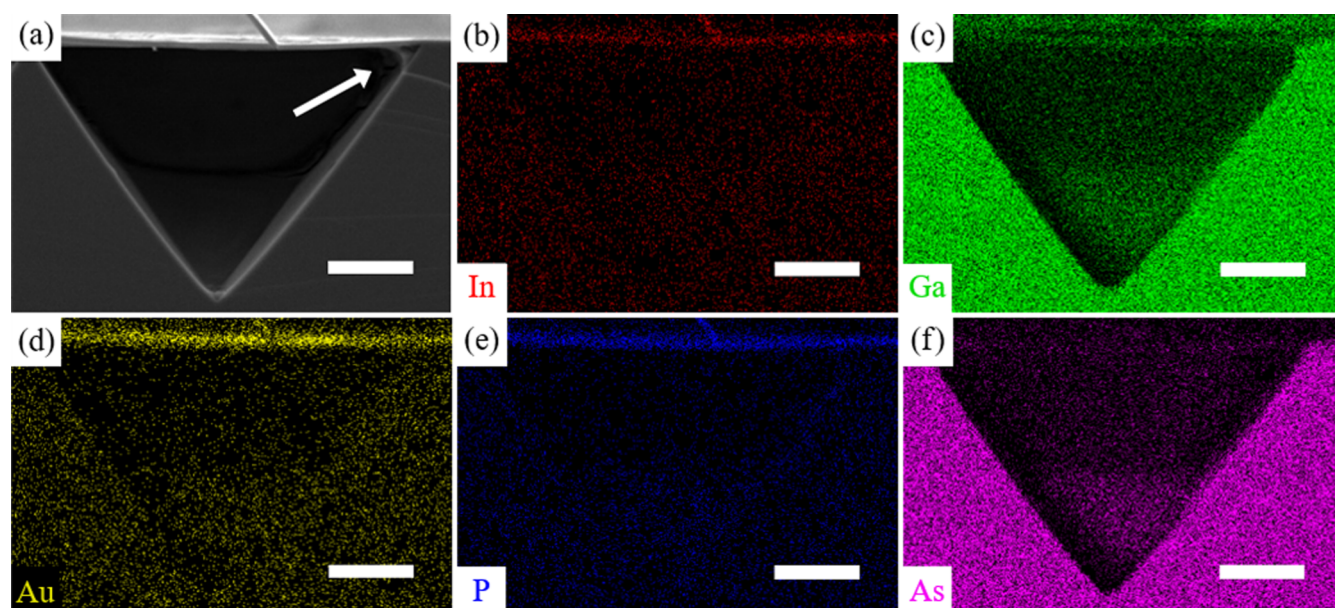
**Figure 5.** (a) Cross-sectional SEM image of Au-patterned i-InGaP nanofoil suspended over a micro-trench in the GaAs substrate after an etching period of 50 min. Corresponding EDXS maps are shown, which are representative of elemental (b) In, (c) Ga, (d) Au, (e) P, and (f) As. The Au-covered InGaP nanofoil is prominently observed in panels (b)−(e), while absent in the elemental As map (f). The white arrow points to the re-entrant profile formed in the GaAs substrate. All scale bars represent 3 $\mu$m.

extend beneath the InGaP layer (shown as the light gray film in Figure 6b) and into the GaAs substrate (dark gray). Moreover, an overlap of the neighboring distributions at the midpoint between two Au features marks the location of enhanced I-MacEtch and corresponds to the site of cavity formation in the InGaP layer. Figure 6c represents the features generated in the oxidized GaAs substrate after the cavity formation and when HF has penetrated the InGaP layer (note: the viewing plane in Figure 6c corresponds to the center of the off-metal window, and simply depicts a row of neighboring features; thus, no features from background rows are observed, unlike those seen in Figure 4c). The InGaP layer acts as a patterned mask for the rapid etching of the oxidized GaAs regions near the interface and deeper substrate regions along the {111} planes. The position of the cavity in the InGaP layer is aligned with the initial GaAs etching location and corresponds to the bottom of the inverse pyramidal micro-trench that is etched in the GaAs substrate. Thus, the mesh-patterned Au catalyst enables I-MacEtch of the InGaP layer, but also determines the location at which GaAs etching is initiated. The morphology of the micro-trenches formed in the GaAs substrate is not expected to vary with changes in the dimensions of the Au catalyst pattern. Dissolution of GaAs beneath the InGaP window also causes the InGaP nanofoil to be suspended over the micro-trench.

The unique suspended InGaP nanofoil structures described here demonstrate that differential oxidation and dissolution rates can be exploited during I-MacEtch of III−V hetero-structures for single-step nanofabrication of complex architectures. It is anticipated that this process can be exploited for the fabrication of nanoscale, three-dimensional heterostructure geometries for device applications in photonics (e.g., wave-guides), photovoltaics (e.g., tandem-junction solar cells), optoelectronics (e.g., lasers), and nanoelectronics (e.g., HEMTs). In future work, additional structural characterization via transmission electron microscopy (TEM) and chemical analysis via X-ray photoelectron spectroscopy (XPS) and/or Auger electron spectroscopy (AES) is required to understand

the basis of the I-MacEtch mechanism, specifically related to the potential absence of the distinct oxide phase that was observed at the metal/semiconductor interface in the case of InP I-MacEtch. The nature of a suspended catalyst profile, observed previously for GaP and InP, in comparison to the current conformal Au profile can likewise be investing via TEM in future efforts, which would also identify potential crystallo-graphic dependences at the etch front. Lastly, further investigation of etching rate dependences upon dissimilar micron-scale Au mesh dimensions and exploration of nano-meter-scale catalyst features, which may permit enhanced solution access to oxidized regions and potentially modify the inverse etching behavior observed in the current study, are areas of future consideration.

## 4. CONCLUSIONS

The I-MacEtch behavior of Au-patterned $In_{0.49}Ga_{0.51}P$/GaAs samples in a solution of 14.1 mol/L HF and 6.4 mol/L $H_2O_2$ has been described. Whereas Cr-patterned samples demonstrated no apparent etching behavior, the use of Au-patterned samples under otherwise identical etching conditions led to the formation of suspended InGaP nanofoils over micro-trenches formed in the GaAs substrate, thereby highlighting the catalytic role of Au in the I-MacEtch mechanism. The vertical etch rates for nominally undoped InGaP, p-InGaP, and n-InGaP were determined as 9.7 ± 0.7 nm/min, 8.7 ± 0.6 nm/min, and 8.8 ± 0.9 nm/min, respectively, indicating that etch rates are independent of doping type under the evaluated experimental conditions. The formation of InGaP nanofoils was confirmed via EDXS mapping. A model for the observed I-MacEtch mechanism has been set forth based on overlapping hole distributions in the InGaP layer, which led to localized etching and formation of nanocavities at the center of the off-metal windows, followed by rapid dissolution of the underlying and exposed GaAs substrate. Differential etch rates between the InGaP epilayer and GaAs substrate were exploited in this method for fabrication of suspended InGaP nanofoils of
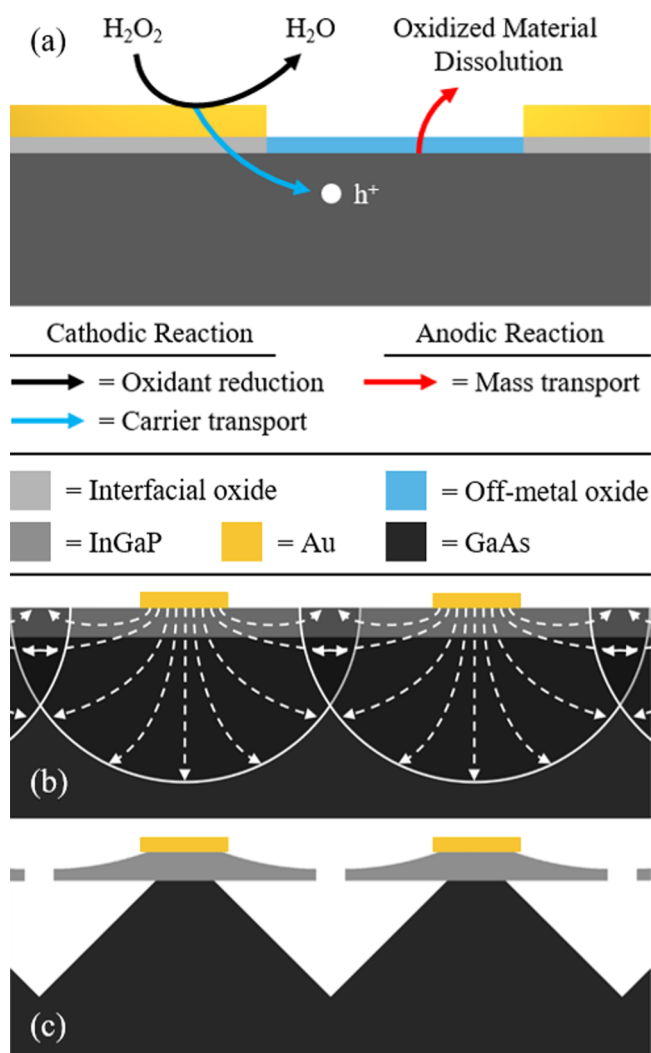
**Figure 6.** Schematics showing (a) the I-MacEtch mechanism and reactions, (b) a qualitative depiction of neighboring hole distributions in the InGaP layer (light gray) and GaAs substrate (dark gray), and (c) a model of the suspended InGaP nanofoil with cavity aligned with the center of the micro-trench generated in the underlying GaAs substrate.

tunable thickness. This technique is anticipated as a practical route toward formation of suspended nanostructures using alternative heteroepitaxial systems, including InGaAs/InP. The I-MacEtch approach described here provides a low-cost method for the fabrication of unique micro- and nanostructures, and does not require the use of hazardous gases, high-temperature processing conditions, or high-vacuum instrumentation. The I-MacEtch process and InGaP nanostructures described in this work may be employed for future device applications in photonics, optoelectronics, photovoltaics, and nanoelectronics.

## ◼ AUTHOR INFORMATION

**Corresponding Author**
*E-mail: pkmohseni@rit.edu.
**ORCID** 
Thomas S. Wilhelm: 0000-0002-2689-0318
Parsian K. Mohseni: 0000-0002-9377-7454

**Notes**
The authors declare no competing financial interest.

## ◼ REFERENCES

(1) Han, H.; Huang, Z.; Lee, W. Metal-Assisted Chemical Etching of Silicon and Nanotechnology Applications. *Nano Today* **2014**, *9*, 271−304.

(2) Irrera, A.; Artoni, P.; Iacona, F.; Pecora, E. F.; Franzò, G.; Galli, M.; Fazio, B.; Boninelli, S.; Priolo, F. Quantum Confinement and Electroluminescence in Ultrathin Silicon Nanowires Fabricated by a Maskless Etching Technique. *Nanotechnology* **2012**, *23*, 075204.

(3) Hochbaum, A. I.; Yang, P. Semiconductor Nanowires for Energy Conversion. *Chem. Rev.* **2010**, *110*, 527−546.

(4) Peng, K.-Q.; Wang, X.; Li, L.; Hu, Y.; Lee, S.-T. Silicon Nanowires for Advanced Energy Conversion and Storage. *Nano Today* **2013**, *8*, 75−97.

(5) Hu, H.; Mohseni, P. K.; Pan, L.; Li, X.; Somnath, S.; Felts, J. R.; Shannon, M. A.; King, W. P. Fabrication of Arbitrarily Shaped Silicon and Silicon Oxide Nanostructures Using Tip-Based Nanofabrication. *J. Vac. Sci. Technol., B: Nanotechnol. Microelectron.: Mater., Process., Meas., Phenom.* **2013**, *31*, 06FJ01.

(6) Li, X. Metal Assisted Chemical Etching for High Aspect Ratio Nanostructures: A Review of Characteristics and Applications in Photovoltaics. *Curr. Opin. Solid State Mater. Sci.* **2012**, *16*, 71−81.

(7) Pinto, R.; Babu, R. S.; Bhattacharya, P. K. Annealing of Si Damage Caused by Reactive Ion Etching in SF6 Gas Mixtures. *Appl. Phys. Lett.* **1986**, *48*, 1427−1429.

(8) Joshi, A. B.; Mann, E.; Chung, L.; Cho, T. H.; Min, B. W.; Kwong, D. L. Reduction of RIE-Damage by N2O-Anneal of Thermal Gate Oxide. *IEEE Transactions on Semiconductor Manufacturing* **1998**, *11*, 495−500.

(9) Huang, Z.; Geyer, N.; Werner, P.; de Boor, J.; Gösele, U. Metal-Assisted Chemical Etching of Silicon: A Review. *Adv. Mater.* **2011**, *23*, 285−308.

(10) Egatz-Gomez, A.; Majithia, R.; Levert, C.; Meissner, K. E. Super-Wetting, Wafer-Sized Silicon Nanowire Surfaces with Hierarchical Roughness and Low Defects. *RSC Adv.* **2012**, *2*, 11472−11480.

(11) Zhang, B.; Wang, H.; Lu, L.; Ai, K.; Zhang, G.; Cheng, X. Large-Area Silver-Coated Silicon Nanowire Arrays for Molecular Sensing Using Surface-Enhanced Raman Spectroscopy. *Adv. Funct. Mater.* **2008**, *18*, 2348−2355.

(12) Chern, W.; Hsu, K.; Chun, I. S.; de Azeredo, B. P.; Ahmed, N.; Kim, K.-H.; Zuo, J.; Fang, N.; Ferreira, P.; Li, X. Nonlithographic Patterning and Metal-Assisted Chemical Etching for Manufacturing of Tunable Light-Emitting Silicon Nanowire Arrays. *Nano Lett.* **2010**, *10*, 1582−1588.

(13) Liu, R.; Zhao, X.; Roberts, C.; Yu, L.; Mohseni, P. K.; Li, X.; Podolskiy, V.; Wasserman, D. Enhanced Optical Transmission through MacEtch-Fabricated Buried Metal Gratings. *Adv. Mater.* **2016**, *28*, 1441−1448.

(14) Mohseni, P. K.; Hyun Kim, S.; Zhao, X.; Balasundaram, K.; Dong Kim, J.; Pan, L.; Rogers, J. A.; Coleman, J. J.; Li, X. GaAs Pillar Array-Based Light Emitting Diodes Fabricated by Metal-Assisted Chemical Etching. *J. Appl. Phys.* **2013**, *114*, 064909.

(15) Qi, Y.; Wang, Z.; Zhang, M.; Wang, X.; Ji, A.; Yang, F. Electron Transport Characteristics of Silicon Nanowires by Metal-Assisted Chemical Etching. *AIP Adv.* **2014**, *4*, 031307.

(16) Song, Y.; Mohseni, P. K.; Kim, S. H.; Shin, J. C.; Ishihara, T.; Adesida, I.; Li, X. Ultra-High Aspect Ratio InP Junctionless FinFETs by a Novel Wet Etching Method. *IEEE Electron Device Lett.* **2016**, *37*, 970−973.

(17) McSweeney, W.; Lotty, O.; Holmes, J. D.; O'Dwyer, C. Fabrication and Characterization of Single-Crystal Metal-Assisted

Chemically Etched Rough Si Nanowires for Lithium-Ion Battery Anodes. *ECS Trans.* **2011**, *35*, 25−34.

(18) Shin, J. C.; Chanda, D.; Chern, W.; Yu, K. J.; Rogers, J. A.; Li, X. Experimental Study of Design Parameters in Silicon Micropillar Array Solar Cells Produced by Soft Lithography and Metal-Assisted Chemical Etching. *IEEE Journal of Photovoltaics* **2012**, *2*, 129−133.

(19) Li, X.; Bohn, P. W. Metal-Assisted Chemical Etching in HF/H2O2 Produces Porous Silicon. *Appl. Phys. Lett.* **2000**, *77*, 2572−2574.

(20) Li, X.; Kim, Y.-W.; Bohn, P. W.; Adesida, I. In-Plane Bandgap Control in Porous GaN through Electroless Wet Chemical Etching. *Appl. Phys. Lett.* **2002**, *80*, 980−982.

(21) Kong, L.; Dasgupta, B.; Ren, Y.; Mohseni, P. K.; Hong, M.; Li, X.; Chim, W. K.; Chiam, S. Y. Evidences for Redox Reaction Driven Charge Transfer and Mass Transport in Metal-Assisted Chemical Etching of Silicon. *Sci. Rep.* **2016**, *6*, 36582.

(22) Miao, B.; Zhang, J.; Ding, X.; Wu, D.; Wu, Y.; Lu, W.; Li, J. Improved Metal Assisted Chemical Etching Method for Uniform, Vertical and Deep Silicon Structure. *J. Micromech. Microeng.* **2017**, *27*, 055019.

(23) Li, M.; Li, Y.; Liu, W.; Yue, L.; Li, R.; Luo, Y.; Trevor, M.; Jiang, B.; Bai, F.; Fu, P.; Zhao, Y.; Shen, C.; Mbengue, J. M. Metal-Assisted Chemical Etching for Designable Monocrystalline Silicon Nanostructure. *Mater. Res. Bull.* **2016**, *76*, 436−449.

(24) Kim, J. D.; Mohseni, P. K.; Balasundaram, K.; Ranganathan, S.; Pachamuthu, J.; Coleman, J. J.; Li, X. Scaling the Aspect Ratio of Nanoscale Closely Packed Silicon Vias by MacEtch: Kinetics of Carrier Generation and Mass Transport. *Adv. Funct. Mater.* **2017**, *27*, 1605614.

(25) Lai, R. A.; Hymel, T. M.; Narasimhan, V. K.; Cui, Y. Schottky Barrier Catalysis Mechanism in Metal-Assisted Chemical Etching of Silicon. *ACS Appl. Mater. Interfaces* **2016**, *8*, 8875−8879.

(26) Geng, X.; Duan, B. K.; Grismer, D. A.; Zhao, L.; Bohn, P. W. Monodisperse GaN Nanowires Prepared by Metal-Assisted Chemical Etching with in Situ Catalyst Deposition. *Electrochem. Commun.* **2012**, *19*, 39−42.

(27) Song, Y.; Oh, J. Fabrication of Three-Dimensional GaAs Antireflective Structures by Metal-Assisted Chemical Etching. *Sol. Energy Mater. Sol. Cells* **2016**, *144*, 159−164.

(28) DeJarld, M.; Shin, J. C.; Chern, W.; Chanda, D.; Balasundaram, K.; Rogers, J. A.; Li, X. Formation of High Aspect Ratio GaAs Nanostructures with Metal-Assisted Chemical Etching. *Nano Lett.* **2011**, *11*, 5259−5263.

(29) Asoh, H.; Imai, R.; Hashimoto, H. Au-Capped GaAs Nanopillar Arrays Fabricated by Metal-Assisted Chemical Etching. *Nanoscale Res. Lett.* **2017**, *12*, 444.

(30) Cheung, H.-Y.; Lin, H.; Xiu, F.; Wang, F.; Yip, S.; Ho, J. C.; Wong, C.-Y. Mechanistic Characteristics of Metal-Assisted Chemical Etching in GaAs. *J. Phys. Chem. C* **2014**, *118*, 6903−6908.

(31) Song, Y.; Ki, B.; Choi, K.; Oh, I.; Oh, J. In-Plane and out-of-Plane Mass Transport during Metal-Assisted Chemical Etching of GaAs. *J. Mater. Chem. A* **2014**, *2*, 11017−11021.

(32) Kim, J.; Oh, J. Formation of GaP Nanocones and Micro-Mesas by Metal-Assisted Chemical Etching. *Phys. Chem. Chem. Phys.* **2016**, *18*, 3402−3408.

(33) Kong, L.; Song, Y.; Kim, J. D.; Yu, L.; Wasserman, D.; Chim, W. K.; Chiam, S. Y.; Li, X. Damage-Free Smooth-Sidewall InGaAs Nanopillar Array by Metal-Assisted Chemical Etching. *ACS Nano* **2017**, *11*, 10193−10205.

(34) Kang, J. H.; Ryu, J. H.; Kim, H. K.; Kim, H. Y.; Han, N.; Park, Y. J.; Uthirakumar, P.; Hong, C.-H. Comparison of Various Surface Textured Layer in InGaN LEDs for High Light Extraction Efficiency. *Opt. Express* **2011**, *19*, 3637−3646.

(35) Cowley, A.; Steele, J. A.; Byrne, D.; Vijayaraghavan, R. K.; McNally, P. J. Fabrication and Characterisation of GaAs Nanopillars Using Nanosphere Lithography and Metal Assisted Chemical Etching. *RSC Adv.* **2016**, *6*, 30468−30473.

(36) Zhang, J.; Zhang, L.; Han, L.; Tian, Z.-W.; Tian, Z.-Q.; Zhan, D. Electrochemical Nanoimprint Lithography: When Nanoimprint

Lithography Meets Metal Assisted Chemical Etching. *Nanoscale* **2017**, *9*, 7476−7482.

(37) Zhou, W.; Min, G.; Zhang, J.; Liu, Y.; Wang, J.; Zhang, Y.; Sun, F. Nanoimprint Lithography: A Processing Technique for Nanofabrication Advancement. *Nano-Micro Lett.* **2011**, *3*, 135−140.

(38) Li, L.; Zhang, G.; Wong, C. P. Formation of Through Silicon Vias for Silicon Interposer in Wafer Level by Metal-Assisted Chemical Etching. *IEEE Trans. Compon., Packag., Manuf. Technol.* **2015**, *5*, 1039−1049.

(39) Nassiopoulou, A. G.; Gianneta, V.; Katsogridakis, C. Si Nanowires by a Single-Step Metal-Assisted Chemical Etching Process on Lithographically Defined Areas: Formation Kinetics. *Nanoscale Res. Lett.* **2011**, *6*, 597.

(40) Rykaczewski, K.; Hildreth, O. J.; Kulkarni, D.; Henry, M. R.; Kim, S.-K.; Wong, C. P.; Tsukruk, V. V.; Fedorov, A. G. Maskless and Resist-Free Rapid Prototyping of Three-Dimensional Structures Through Electron Beam Induced Deposition (EBID) of Carbon in Combination with Metal-Assisted Chemical Etching (MaCE) of Silicon. *ACS Appl. Mater. Interfaces* **2010**, *2*, 969−973.

(41) Chun, I. S.; Chow, E. K.; Li, X. Nanoscale Three Dimensional Pattern Formation in Light Emitting Porous Silicon. *Appl. Phys. Lett.* **2008**, *92*, 191113.

(42) Kim, S. H.; Mohseni, P. K.; Song, Y.; Ishihara, T.; Li, X. Inverse Metal-Assisted Chemical Etching Produces Smooth High Aspect Ratio InP Nanostructures. *Nano Lett.* **2015**, *15*, 641−648.

(43) Lin, H.-C.; Lee, F.-M.; Cheng, Y.-C.; Lee, K.-W.; Adriyanto, F.; Wang, Y.-H. InGaP/InGaAs MOS-PHEMT with a Nanoscale Liquid Phase-Oxidized InGaP Dielectric. *Solid-State Electron.* **2012**, *68*, 27−31.

(44) Chen, C. C.; Chen, H. I.; Chou, P. C.; Liou, J. K.; Chiou, Y. J.; Tsai, J. H.; Liu, W. C. Performance Enhancement on an InGaP/InGaAs PHEMT With an Electrophoretic Deposition Gate Structure. *IEEE Electron Device Lett.* **2014**, *35*, 18−20.

(45) Schulte, K. L.; Simon, J.; Mangum, J.; Packard, C. E.; Gorman, B. P.; Jain, N.; Ptak, A. J. Development of GaInP Solar Cells Grown by Hydride Vapor Phase Epitaxy. *IEEE Journal of Photovoltaics* **2017**, *7*, 1153−1158.

(46) Lu, S.; Ji, L.; He, W.; Dai, P.; Yang, H.; Arimochi, M.; Yoshida, H.; Uchida, S.; Ikeda, M. High-Efficiency GaAs and GaInP Solar Cells Grown by All Solid-State Molecular-Beam-Epitaxy. *Nanoscale Res. Lett.* **2011**, *6*, 576.

(47) Williams, K. R.; Gupta, K.; Wasilik, M. Etch Rates for Micromachining Processing-Part II. *J. Microelectromech. Syst.* **2003**, *12*, 761−778.

(48) Peng, K.; Wu, Y.; Fang, H.; Zhong, X.; Xu, Y.; Zhu, J. Uniform, Axial-Orientation Alignment of One-Dimensional Single-Crystal Silicon Nanostructure Arrays. *Angew. Chem., Int. Ed.* **2005**, *44*, 2737−2742.

(49) Huang, J.; Chiam, S. Y.; Tan, H. H.; Wang, S.; Chim, W. K. Fabrication of Silicon Nanowires with Precise Diameter Control Using Metal Nanodot Arrays as a Hard Mask Blocking Material in Chemical Etching. *Chem. Mater.* **2010**, *22*, 4111−4116.

(50) Huang, Q.; Ye, Z.; Xiao, X. Recent Progress in Photocathodes for Hydrogen Evolution. *J. Mater. Chem. A* **2015**, *3*, 15824−15837.

(51) Lee, A. R.; Kim, J.; Choi, S.-H.; Shin, J. C. Formation of Three-Dimensional GaAs Microstructures by Combination of Wet and Metal-Assisted Chemical Etching. *Phys. Status Solidi RRL* **2014**, *8*, 345−348.

(52) Takebe, T.; Yamamoto, T.; Fujii, M.; Kobayashi, K. Fundamental Selective Etching Characteristics of HF + H 2 O 2 + H 2 O Mixtures for GaAs. *J. Electrochem. Soc.* **1993**, *140*, 1169−1180.